



# Electron thermodynamics along magnetic nozzle lines in a helicon plasma

Alfio Vinci, Quentin Delavière-Delion, Stéphane Mazouffre

## ► To cite this version:

Alfio Vinci, Quentin Delavière-Delion, Stéphane Mazouffre. Electron thermodynamics along magnetic nozzle lines in a helicon plasma. *Journal of Electric Propulsion*, 2022, 1 (1), pp.4. 10.1007/s44205-022-00003-0 . hal-03629442

**HAL Id: hal-03629442**

**<https://hal.science/hal-03629442>**

Submitted on 4 Apr 2022

**HAL** is a multi-disciplinary open access archive for the deposit and dissemination of scientific research documents, whether they are published or not. The documents may come from teaching and research institutions in France or abroad, or from public or private research centers.

L'archive ouverte pluridisciplinaire **HAL**, est destinée au dépôt et à la diffusion de documents scientifiques de niveau recherche, publiés ou non, émanant des établissements d'enseignement et de recherche français ou étrangers, des laboratoires publics ou privés.

RESEARCH

Open Access



# Electron thermodynamics along magnetic nozzle lines in a helicon plasma

Alfio E. Vinci<sup>\*</sup>, Quentin Delavière–Delion and Stéphane Mazouffre

<sup>\*</sup>Correspondence:

alfio.vinci@cnsr-orleans.fr  
Institut de Combustion,  
Aérothermique, Réactivité et  
Environnement (ICARE), Centre  
National de la Recherche  
Scientifique (CNRS), 1C Avenue de  
la Recherche Scientifique, Orléans  
45071, France

## Abstract

The electron cooling rate is experimentally investigated along the magnetic lines of a helicon plasma device operating with different magnetic nozzle shapes. Probe measurements in a 2-D region of the plasma plume outline that the polytropic index of electrons has dissimilar values along distinct streamlines ranging from  $\gamma_e \simeq 1.4$  to  $\gamma_e > 1.8$ . Accounting for ionization phenomena as an additional degree of freedom allows to predict a polytropic index smaller than the adiabatic limit. It is observed that a reduced cross-field transport can effectively reduce the electrons degrees of freedom.

**Keywords:** Magnetic nozzle, Electron thermodynamics, Polytropic index, Helicon plasma

## Introduction

Electrodeless plasma thrusters and magnetic nozzles (MN) offer certain advantages compared to state-of-the-art systems for the purpose of producing thrust in space. Several research groups are currently engaged in experimental [1–7] and numerical [8–10] studies in order to deepen the physical understanding of this technology with the primary aim of improving the propulsive performance. A magnetic nozzle consists in an externally applied steady magnetic field with convergent-divergent or divergent only geometry which enables the transport and acceleration of ions up to supersonic speeds into vacuum. Most of the exploited kind of electrodeless devices, e.g. helicon plasma thrusters (HPT) and electron cyclotron resonance thrusters (ECRT), integrate a MN to increase the momentum of the ejected ions. Qualities like a current-free nature, the withdrawal of plasma-electrodes interaction, the design simplicity, are the asset of this technology which can nominally operate without a dedicated neutralizer and on virtually any propellant.

A number of transport phenomena are seen to occur in a MN as the result of inlet thermal energy usually stored in the electron population, such as an ambipolar electric diffusion [11] and an azimuthal diamagnetic electron current [12]. Both of them act in converting the electron energy in ion kinetic energy, the former as an electrostatic force term and the latter as an electromagnetic contribution. Consequently, the rate at which the electron cooling occurs throughout the MN represents a pivotal element in the far-field plasma dynamics in terms of energy and momentum transfer. Furthermore, the

plasma flow detachment from the magnetic field lines is possibly just as impacted by the electron cooling process [13].

Several experimental studies have been performed to measure the effective electron polytropic index along the axis of the MN. Little and Choueiri [14] observed that the electrons cooling occurs with an exponent equal to  $1.15 \pm 0.03$  in their rf plasma device regardless of the applied magnetic field strength. In a collisional regime with Maxwellian electrons, this intermediate value between the isothermal and adiabatic cases has been attributed to a Nusselt number  $Nu \ll 1$  in their plume, i.e. a dominant conductive electron heat flux. Zhang et al. [15] found a polytropic index of  $1.17 \pm 0.02$  in their low density helicon plasma plume. In their primarily collisionless case, observation of strongly non-Maxwellian electron distribution functions led to the conclusion that the measured polytropic index, although smaller than  $5/3$ , describes an adiabatic expansion in a plume far from local thermodynamic equilibrium. Takahashi et al. [16] and later Kim et al. [17] studied the electron thermodynamics in the MN linked to similar plasma sources that used a filament cathode. The findings in [16] showed a continuous change of the polytropic index along the MN axis, with its variation depending on the magnetic field strength. This has raised the idea that an adiabatic expansion occurs when a strong magnetic field constrains the cross-field diffusion through the spontaneous onset of a radial electric field in the plasma. In [17], these results are further expanded observing a polytropic index close to 2 which is not affected by the magnetic field strength whenever the axial and radial electric fields remain unchanged.

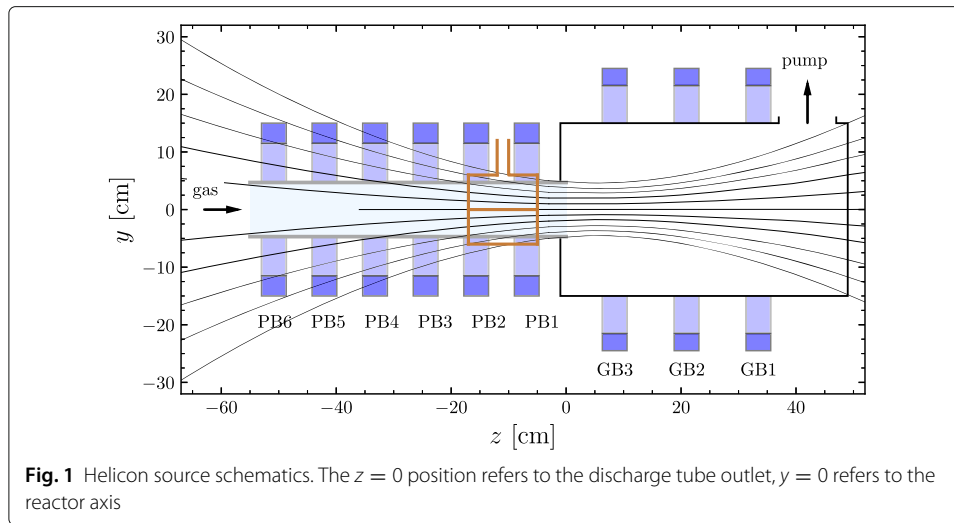
In this scenario, a 2-D picture of the electron thermodynamics in a MN remains entirely unexplored. Given that the radial distribution of the plasma properties is typically far from being homogeneous, it is expected that the polytropic index measured on-axis not necessarily retains its value elsewhere in the plume. The availability of experimental data in this regard is of particular interest for the development of predictive numerical model such those discussed in [8, 13]. To this end, the present paper reports on 2-D measurements of the electron cooling rate retrieved along the magnetic streamlines in three different magnetic nozzle shapes. Plasma density and electron temperature are spatially resolved in the magnetic nozzle of a helicon device and afterwards correlated to compute the polytropic index under the hypotheses of negligible electron inertia and fully magnetized electrons. A detailed description of the experimental setup is provided in [Experimental setup](#) section, which includes the helicon source and the diagnostics used to probe the plasma properties. Results are presented and discussed in [Results and discussion](#) section. Eventually, conclusions are drawn in [Conclusion](#) section.

## Experimental setup

### Helicon plasma source

The HP source employed in this study has been previously described in [6, 7]. It is schematically shown in Fig. 1 along with an example of computed magnetic streamlines. The whole experimental setup is oriented in a vertical position.

The tube constituting the discharge chamber is made in borosilicate glass with  $\phi = 9.4$  cm inner diameter and  $L = 55$  cm length. The origin of the axial coordinate  $z$  is arbitrarily defined to coincide with the tube open boundary. Xenon gas is introduced off-axis at the injection plate of the reactor which is placed at the top aperture of the glass tube. The gas goes through a plenum first and eventually reaches the discharge chamber



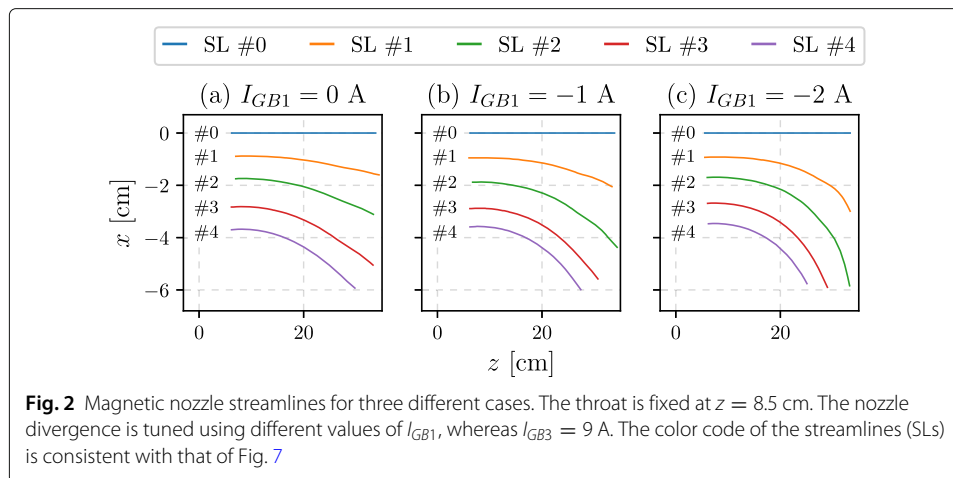
via a multi-perforated plate, resulting in an axial gas flow. In this study, the flow rate is fixed to  $0.2 \pm 0.003 \text{ mg s}^{-1}$ . The bottom part is connected to a 30 cm in inner diameter and 50 cm in length expansion chamber made in aluminum which is equipped with a turbo-molecular/primary pumping system. The ultimate base pressure is in the order of  $10^{-5}$  mbar, whereas the typical pressure during operation reads about  $10^{-3}$  mbar.

The rf antenna in use is a double-saddle type with 12 cm length centered at  $z \cong -11$  cm. It is made of pure copper and is directly connected to a custom  $\pi$ -type matching network. Input rf power is generated by a 1 kW-class commercial power supply at 13.56 MHz and kept constant to 800 W for the measurements herein reported. Matching of the rf power is manually attained and the reflected power is typically below 1% during operation. The helicon-mode regime has been experimentally verified in [6] for similar operating conditions.

Nine electromagnets surround both the discharge and expansion chambers. Figure 1 reports their location and denomination. Each electromagnet is made up of a 2 mm diameter copper wire, constituting 510 loops for PB1-6 and 430 loops for GB1-3. The current flowing in each electromagnet can be tuned in order to achieve the desired topology of the external magnetic field. In this experiment, GB1 and GB3 are solely used to exploit three different divergent shapes of the magnetic nozzle. The current dedicated to GB3, i.e.  $I_{GB3}$ , is fixed to +9 A, whereas  $I_{GB1}$  is set to 0 A, -1 A and -2 A. A positive (negative) value of the current means that the generated  $\mathbf{B}$  field points along the  $+z$  ( $-z$ ) direction. In all of the three studied MNs, the peak value of the axial magnetic field reads  $8.6 \pm 0.3$  mT in correspondence of GB3 at  $z \simeq 8$  cm. Table 1 schematically reproduces the three tested configurations. Each set of currents generates a different shape of the MN whose divergence increases together with the absolute value of  $I_{GB1}$ . The streamlines identifying the tested MNs are represented in Fig. 2. Every streamline (SL) is numbered and associated with a color which is used afterward for the interpretation of measurement outcomes.

**Table 1** Electromagnets current for the three magnetic configurations in analysis

	MN config.(a)	MN config.(b)	MN config.(c)
$I_{GB1}$	0 A	-1 A	-2 A
$I_{GB3}$	+9 A	+9 A	+9 A



The numbering is also included beside each SL within the plots for the sake of clarity. As an example, the on-axis SL is numbered #0 and associated with the blue color, cf. Fig. 2.

### Diagnostics

With the purpose of studying the electron thermodynamics, the local electron density and temperature are measured using the rf-compensated Langmuir probe (LP) depicted in Fig. 3. A comprehensive technical description of the probe has been previously reported in [6]. The probe design is based on the results and guidelines reported in [18]. The tip of the probe is a 0.38 mm diameter and 5 mm tungsten wire. An additional compensating electrode made of stainless steel is connected in parallel to the tip through a 1 nF axial capacitor and it provides mechanical support to the whole assembly as well. A series of three axial chokes, each of which self-resonates at one of the first three harmonics, ensures the proper rf compensation of the probe [6].

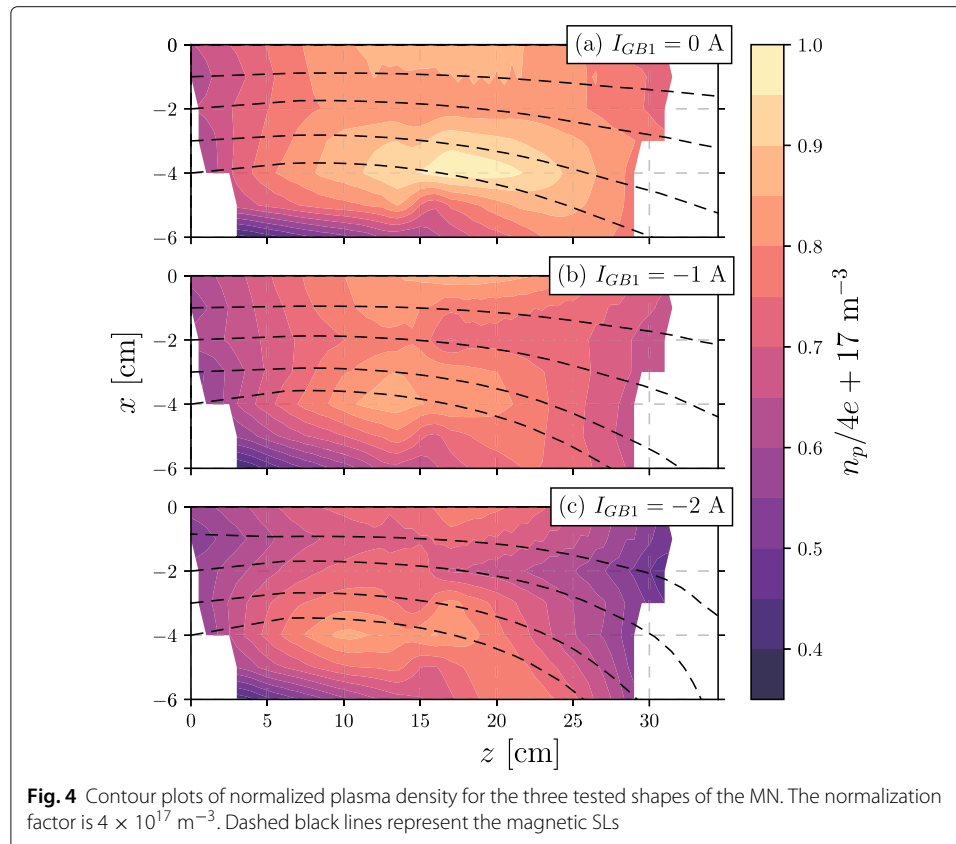
The LP is manually actuated within the measurement region using a single-axis translation stage with a resolution of 10  $\mu\text{m}$  and a stroke of 150 mm. The probe is aligned by means of a cross-line laser pendulum with an uncertainty of about 5 mm on its position. I-V curves are recorded using an Automated Langmuir Probe control unit by Impedans Ltd. Eventually, plasma parameters are deduced using the orbital motion limited (OML) theory [19, 20]. Assuming the plasma is locally quasi-neutral, the electron/plasma density  $n_p$  is retrieved from the linear fit of the ion current squared versus the probe bias potential. Then, the electron current is computed by subtracting the ion current fit from the total probe current. Under the assumption of a Maxwell-Boltzmann electron distribution function, the electron temperature  $T_e$  is inferred from the linear fit of the electron current logarithmic profile versus the probe bias potential. Alternatively,  $T_e$  can be estimated from the electron energy probability function (EEPF) computed using the Druyvesteyn method [21], providing comparable results. The plasma potential  $V_p$  is computed as the probe bias voltage where the first derivative of the I-V curve features its peak value.

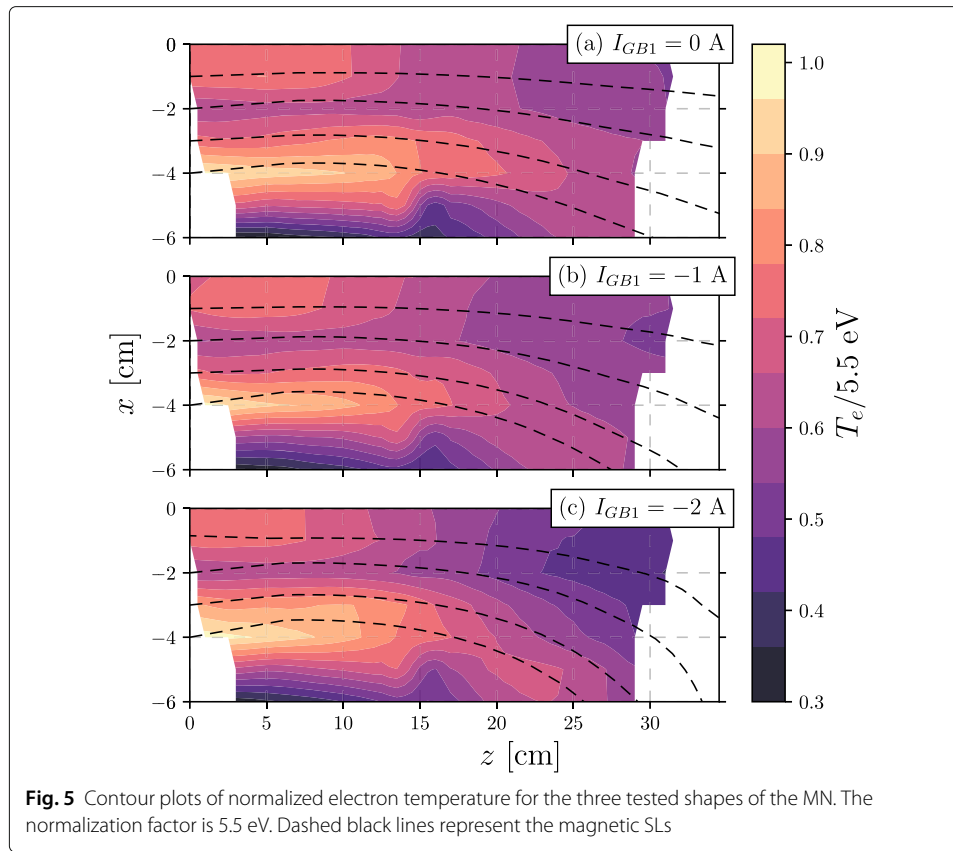


The random uncertainty associated with the probe measurements has been statistically estimated in [6], outlining that  $n_p$  and  $T_e$  have a typical statistical deviation below 1%. However, systematic errors associated with LP measurements are commonly larger. These errors, which are virtually impossible to evaluate, clearly impact the determination of  $\gamma_e$  whatever the plasma source or experimental conditions in general. In this specific case, the issue of uncertainties might be especially important since the expansion area studied here is relatively small compared to other experimental studies on electron cooling [14, 16, 17]. As a result, the determination of  $\gamma_e$  may be relatively more sensitive to  $n_p$  and  $T_e$  uncertainties.

## Results and discussion

For the purpose of studying the electron thermodynamics along the magnetic SLs, the rf-compensated LP described in [Diagnostics](#) section is displaced in the region  $-6 < x < 0$  cm and  $0 < z < 30$  cm to resolve the electron properties. The I-V curves are recorded with a spatial resolution of 5 mm along  $z$  and 10 mm along  $x$ . Data post-processing involved the use of OML theory to retrieve  $n_p$  and  $T_e$ , along with a smoothing algorithm based on a dynamic Savitzky-Golay filter. The resulting normalized  $(x - z)$  profiles of  $n_p$  and  $T_e$  are shown in Figs. 4 and 5, respectively. Normalization factors are  $4 \times 10^{17} \text{ m}^{-3}$  for  $n_p$  and 5.5 eV for  $T_e$ . The dashed black lines included in each plot reproduce the magnetic SLs as previously displayed in Fig. 2. Figure 4 shows that the expanding plasma features a high density region along the HP source axis along with high density conics, which are often observed in other experiments [4, 7, 22]. In the  $z \lesssim 10$  cm domain, the density





increases due to the increasing magnitude of the external magnetic field. Regardless of the MN shape, the highest value of  $n_p$  is located off-axis. Yet, the density peak moves upstream as the MN divergence is increased. As a matter of fact, with reference to Fig. 4, the maximum of  $n_p$  is observed at (a)  $z \simeq 17$  cm, (b)  $z \simeq 13$  cm and (c)  $z \simeq 10$  cm. A positive density gradient beyond the magnetic throat is likely linked to pressure balance effects as analyzed in [6] where the plasma source was operated under similar conditions. Furthermore, the spatial evolution of the high density conics largely resembles the shape of the MN, highlighting that the electrons are visibly magnetized in all of the studied configurations.

Similar comments can be drawn concerning the electron temperature profiles in Fig. 5. Relatively higher temperature electrons are localized on-axis and at the external surface of the MN.  $T_e$  is larger in the latter region regardless of the MN shape. Some works associate the presence of higher energy electrons at the edge of the MN to heating phenomena near the rf antenna and transport along the SLs [23]. The region at  $z \lesssim 10$  cm is visibly unchanged albeit the MN is differently shaped, cf. Fig. 5(a-c). It suggests that the discharge process inside the source tube is not deeply influenced by the downstream conditions. At  $z > 10$  cm, in contrast, the maps of  $T_e$  exhibit important dissimilarities owing to the different shape of the MN. Consistently to what is observed in Fig. 4, the spatial evolution of  $T_e$  similarly resembles the computed magnetic SLs, further hinting that the electrons are strongly magnetized.

The data mapped in the MN as shown in Figs. 4 and 5 is used for a more detailed

analysis of the electron flow properties. The evolution of the electrons is often modeled with a polytropic state equation,

$$T_e/n_p^{\gamma_e-1} = C(\psi) \quad (1)$$

where  $\gamma_e$  is the polytropic index and  $C$  is constant along a characteristic magnetic surface  $\psi$ . Note that  $T_e$  is in general an effective value of the electron energy. In the present case,  $T_e$  can be computed as discussed in [Diagnostics](#) section since the EEPF remains nearly Maxwellian as exemplified in [Fig. 6](#). Assuming that the electron inertia is negligible and the electrons are fully magnetized, the magnetic SLs coincide with the electron flow SLs [\[13\]](#). Hence, the polytropic law is evaluated along the  $(x, z)$  coordinates that define the computed magnetic SLs. In order to evaluate  $(n_p, T_e)$  at the exact same point  $[x, z]$  belonging to the magnetic SL, the experimental maps are numerically interpolated by means of a linear method. Given that  $n_p$  increases in the upstream portion of the probed domain, cf. [Fig. 4](#), the data of this region is disregarded. In other terms, only the region where  $\nabla n_p < 0$  is considered as the focus here is to analyze the expansion process. Eventually, the polytropic index  $\gamma_e$  is inferred using a linear regression of the  $\log_{10}(T_e)$  vs.  $\log_{10}(n_p)$  datasets. [Figure 7](#) gathers the results obtained evaluating  $\gamma_e$  along the magnetic SLs previously shown in [Fig. 2](#) for each of the studied MN shapes. The colors in [Fig. 7](#) are consistent with those in [Fig. 2](#), thus allowing to identify the magnetic SL that corresponds to each set of scatter points and fitting lines.

Interestingly,  $\gamma_e$  has dissimilar values along distinct SLs. Furthermore, in some cases it reads  $\gamma_e > 5/3$  (adiabatic value with  $N = 3$  degrees of freedom) and each of the magnetic nozzles being tested features a unique structure of  $\gamma_e$ . Indeed, as evident from [Fig. 7\(a\)](#), the polytropic index in the first MN ranges from  $\gamma_e \simeq 1.3$  along SL#2 to  $\gamma_e \simeq 1.8$  along SL#0 and SL#4. In [Fig. 7\(b\)](#), instead, the smallest value  $\gamma_e \simeq 1.4$  is found along SL#0 and SL#1 whereas the maximum  $\gamma_e \simeq 1.8$  occurs along SL#3 and SL#4. [Figure 7\(c\)](#) manifests a further different case in which  $\gamma_e \simeq 1.4 - 1.5$  regardless of the SL. The cases  $\gamma_e \simeq 2$  imply that the degrees of freedom of electrons can be reduced to 2, while  $\gamma_e < 5/3$  would suggest the presence of heat flux within the MN under the hypothesis of local thermodynamic equilibrium (LTE). The study reported in [\[15\]](#) shows that strongly non-Maxwellian EEPF yields an adiabatic expansion with  $\gamma_e \simeq 1.17$  in a collisionless regime. However, nearly Maxwellian electrons are found in the present experiment thereby collisionless phenomena are not of primary relevance here. Moreover, the theory developed in [\[14\]](#) fails to predict the values of  $\gamma_e$  observed in this experiment. By using the Spitzer resistivity [\[24\]](#)

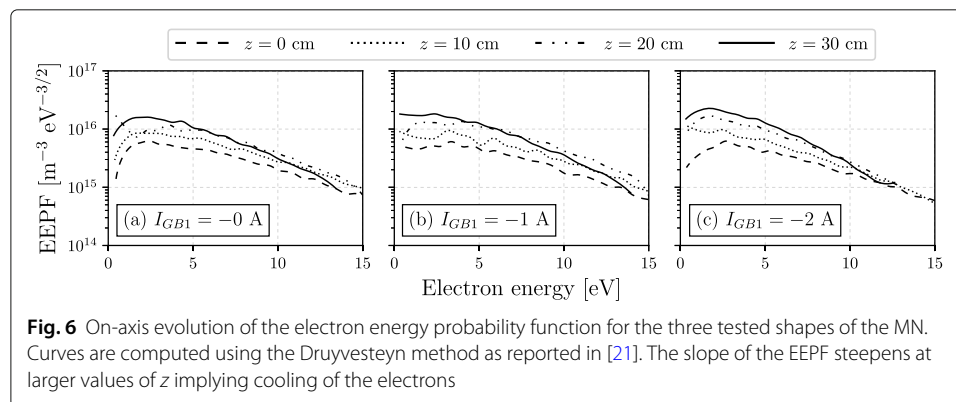
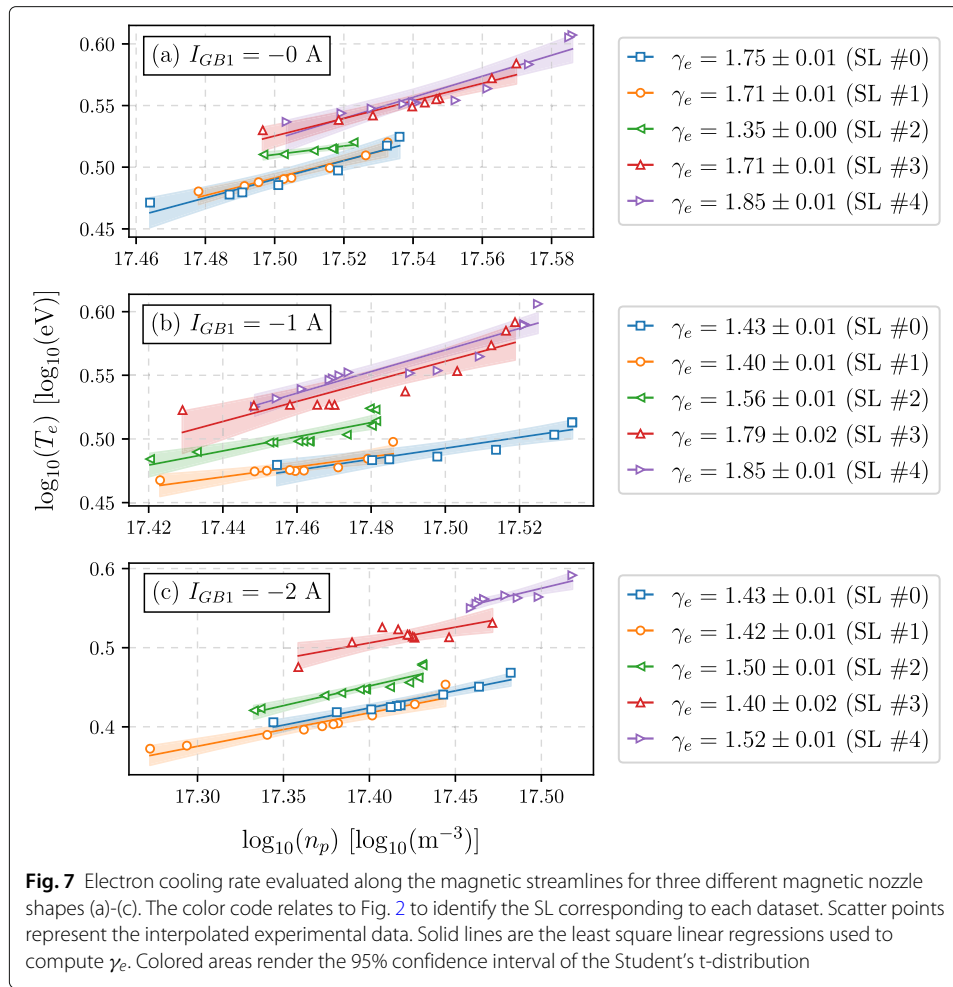


**Fig. 6** On-axis evolution of the electron energy probability function for the three tested shapes of the MN. Curves are computed using the Druyvesteyn method as reported in [\[21\]](#). The slope of the EEPF steepens at larger values of  $z$  implying cooling of the electrons



for the thermal conductivity, the estimation of the Nusselt number based on the experimental data yields  $Nu \sim 10^{-3}$ . This would translate into  $\gamma_e \approx 1.2$  according to [14] which does not agree with the actual observations. Burm et al. [25] suggest that the ionization process serves as an additional degree of freedom in plasma adiabatic expansions. Using the formulation provided in [25] for a monoatomic plasma in non-LTE, i.e.  $T_i \neq T_e$  and different ionization degree with respect to Saha equilibrium, the value of  $\gamma_e$  is computed as

$$\gamma_e = \frac{c_p}{c_V} \frac{2\Theta + (1 - \Theta)\alpha}{2\Theta + (1 - \Theta)\alpha + (1 - \alpha)\alpha} \quad (2)$$

where  $\Theta = T_i/T_e$  is the ions to electrons temperatures ratio and  $\alpha = n_p/n_n$  is the plasma to neutrals density ratio. The expressions for the heat capacity at constant pressure  $c_p$  and constant volume  $c_V$  read [25]

$$c_p = \frac{5}{2} \frac{R}{\Theta} (\Theta + \alpha) + \frac{\alpha R}{\Theta} \frac{(1 - \alpha)(\Theta + \alpha)}{2\Theta + (1 - \Theta)\alpha} \left( \frac{5}{2} + \frac{\varepsilon_{ion}}{k_B T_e} \right)^2 \quad (3)$$

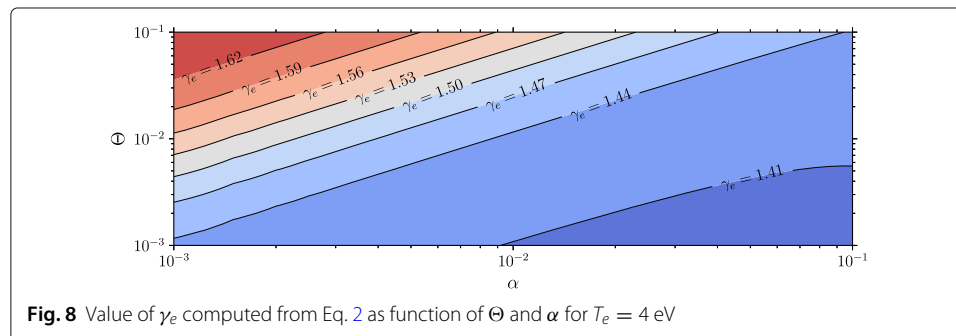
$$c_V = \frac{3}{2} \frac{R}{\Theta} (\Theta + \alpha) + \frac{\alpha R}{\Theta} \frac{(1 - \alpha)(\Theta + \alpha)}{2\Theta + (1 - \Theta)\alpha + (1 - \alpha)\alpha} \left( \frac{3}{2} + \frac{\varepsilon_{ion}}{k_B T_e} \right)^2 \quad (4)$$

where  $R$  is the universal gas constant and  $\varepsilon_{ion}$  is the first ionization energy of the propellant. The implementation of this theory yields  $\gamma_e \simeq 1.3 - 1.5$  for  $T_e = 3 - 6$  eV on the

basis that  $\Theta \sim 10^{-2}$  and  $\alpha \sim 10^{-2}$  in the present experiment. However, the result of Eq. 2 is not dramatically affected by small variations in  $\Theta$  and  $\alpha$  compared to the fitting confidence intervals in Fig. 7, as exemplified in Fig. 8. This means that very dissimilar values of  $\gamma_e$  in this experiment cannot be attributed to small local variations in  $\Theta$  or  $\alpha$ . The value of the polytropic index computed with Eq. 2 agrees well with most of the findings shown beforehand in Fig. 7. This effectively suggests that ionization within the plume does occur, as previously pointed out in other experiments using a MN [7, 26] and Hall thrusters [27]. Nonetheless, this scenario might not be representative in the far-field region. As collision frequencies drop and  $\alpha$  approaches unity, other phenomena besides ionization such as collisionless cooling [28] likely become predominant.

Although the ionization process can clarify the occurrence of  $\gamma_e < 5/3$ , the physical phenomenon that makes  $\gamma_e > 5/3$  has to be investigated. In a simplified picture, the dynamics of electrons in the MN primarily results from the forces associated with the external magnetic field and the spontaneous electric field. As hinted in [16, 17], the radial electric field in the plasma can profoundly affect the transport across the magnetic lines. In [17], relatively high potential regions concentrated off-axis identify a radial electric field which effectively withdraw the degree of freedom related to the motion perpendicular to  $\mathbf{B}$ . A correlation between the radial  $V_p$  and  $\gamma_e$  is therefore requested in the present experiments. The profile of  $V_p$  at  $z = 20$  cm is retrieved from the measured I-V curves and smoothed as shown in Fig. 9(top) for the three shapes of the MN. By determining the radial coordinate where each magnetic SL crosses the section at  $z = 20$  cm, the resulting  $V_p$  and  $\gamma_e$  radial profiles are compared in Fig. 9(bottom). It is found that the two quantities follow a similar qualitative trend along the  $x$  axis. As  $V_p$  experiences a relatively large variation in the radial direction, so does  $\gamma_e$ , cf. Fig. 9(a)-(b). Likewise, a nearly flat profile of  $V_p$  produces a small variation in  $\gamma_e$ , as shown in Fig. 9(c). At this stage, two points shall be addressed when comparing the studied MNs: (i) the different behavior of  $\gamma_e$  in the proximity of the MN axis; (ii) the relatively large  $\gamma_e$  close to the plasma potential peak. The formulation of a comprehensive theory is beyond the purpose of this paper, hence only a few possible explanations are provided in the following.

A value of  $\gamma_e > 5/3$  close to  $x = 0$  is found only for the first MN, cf. Fig. 9(a). This is possibly linked to a more intense magnetic field considering that  $\|\mathbf{B}\| \approx B_z$  spans from about 6 mT in case (a) down to 4 mT in case (c). Differently, an increase in  $\gamma_e$  along with  $V_p$  is observed in all cases of Fig. 9(bottom), reaching  $\gamma_e \simeq 1.7 - 1.9$  in Fig. 9(a-b). A larger  $\gamma_e$  where  $V_p$  is higher seems at odds with the claims in [16, 17]. In the region where the plasma potential is large, rather than owing to the radial electric field, the



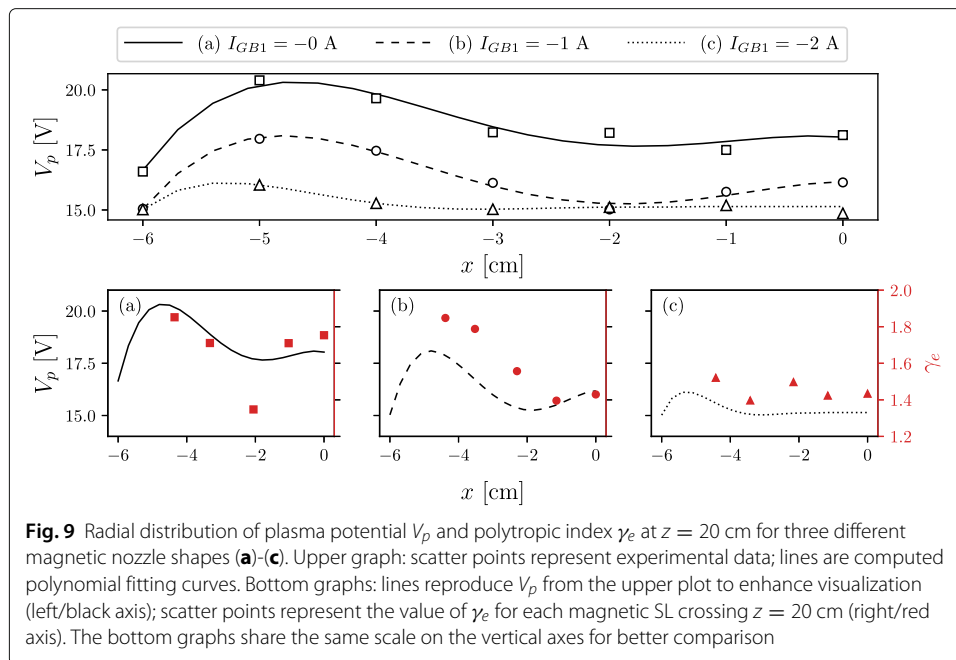


**Fig. 9** Radial distribution of plasma potential  $V_p$  and polytropic index  $\gamma_e$  at  $z = 20$  cm for three different magnetic nozzle shapes (a)-(c). Upper graph: scatter points represent experimental data; lines are computed polynomial fitting curves. Bottom graphs: lines reproduce  $V_p$  from the upper plot to enhance visualization (left/black axis); scatter points represent the value of  $\gamma_e$  for each magnetic SL crossing  $z = 20$  cm (right/red axis). The bottom graphs share the same scale on the vertical axes for better comparison

cross-field electron transport is more likely reduced because a large conductivity ensues in the direction parallel to  $\mathbf{B}$  which strongly promotes the longitudinal transport. This is supported by considering that  $T_e$  is higher where  $V_p$  is larger and that the cross-field diffusion coefficient  $D_\perp \sim (k_B T_e)^{-1/2}$  [24], therefore  $D_\perp$  decreases in the high temperature region. It is worth stressing that  $\gamma_e \simeq 2$  implies a 2-D electron motion, which is therefore reduced to transport along the  $\mathbf{B}$  lines and rotation around them. In extension to the results reported in [16, 17], the present findings suggest that the analysis of the electron cooling dynamics in a MN cannot be addressed regardless of the plasma properties radial profiles throughout the nozzle inlet which are in turn linked to the discharge process.

Nevertheless, it must be emphasized that under the hypothesis of a single isotropic electron fluid, the magnetic field cannot directly modify the number of degrees of freedom [29, 30]. The latter are instead determined by the kinetic nature of the dynamics. The presence of the external magnetic field would contribute to the complexity of the species dynamics, i.e. multiple populations, instabilities and anisotropies might arise thus turning the original assumption behind the concept of  $\gamma_e$  unrealistic. These phenomena and their occurrence are still not fully understood, therefore new and more detailed experimental evidence shall be sought.

Ultimately, a comment is due with regards to the boundary conditions of the plasma studied in this experiment. The interaction between the plasma plume and the vacuum chamber is typically unimportant. However, the diameter of the expansion chamber is about twice that of the plasma column in this case. The metallic walls of the chamber represent both a constant zero-potential boundary and a conductive medium within which closure of internal plasma currents can in principle occur. The latter effect might affect the internal plume structure. Furthermore, the plasma may be thermally connected to the relatively cold walls, thus implying the presence of a heat flux towards the system boundaries. In this experiment, plasma properties are intentionally inferred within a relatively

small domain away from the chamber walls in order to downplay all of the aforementioned effects. Yet, their quantitative assessment represents a further challenge in the experimental process which definitely deserves future investigation.

## Conclusion

The electron cooling rate is experimentally analyzed along the magnetic streamlines of a helicon plasma device while the shape of the magnetic nozzle is varied. The simplest scenario describing an electron flow with 3 degrees of freedom does not provide an accurate picture of the plasma expansion in the present experiment. The introduction of the ionization as an additional degree of freedom allows to better predict the value of the polytropic index for some plasma conditions. In general, the electron polytropic index is observed to be inhomogeneous in space, which emphasizes the prevailing complexities of the MN expansion mechanisms. It is observed that a reduced cross-field transport possibly due to a large longitudinal conductivity can effectively reduce the electrons degrees of freedom (from 3 to 2).

This work represents a first effort in investigating the electron cooling process in a 2-D domain, therefore going beyond the routine analysis performed along the MN axis. The results herein reported are deemed of relevant interest for the purpose of predictive modeling. Nevertheless, additional experimental studies shall be addressed on different kind of devices, e.g. electron cyclotron resonance thrusters, as well as on different scales in order to better identify the phenomena driving the electron cooling dynamics in a magnetic nozzle.

## Acknowledgments

This project has received funding from the European Union's Horizon 2020 research and innovation program under grant agreement No 870542 (Helicon Plasma Thruster for In-space Applications).

## Authors' contributions

A. E. Vinci and S. Mazouffre contributed to the study conception and design. Material preparation and data collection were performed by A. E. Vinci and Q. Delavière–Delion. Data analysis was performed by A. E. Vinci. The first draft of the manuscript was written by A. E. Vinci and all authors commented on previous versions of the manuscript. All authors read and approved the final manuscript.

## Availability of data and materials

The datasets generated during and/or analyzed during the current study are available from the corresponding author on reasonable request.

## Declarations

### Competing interests

The authors declare that they have no competing interests.

Received: 17 December 2021 Accepted: 18 March 2022

Published online: 04 April 2022

## References

1. Wachs B, Jorns B (2020) Background pressure effects on ion dynamics in a low-power magnetic nozzle thruster. *Plasma Sources Sci Technol* 29(4). <https://doi.org/10.1088/1361-6595/ab74b6>
2. Romano F, Herdrich G, Traub C, Fasoulas S, Crisp N, Edmondson S, Haigh S, Livadiotti S, Oiko VTA, Sinpetru LA, Smith K, Becedas J, Bisgaard M, Christensen S, Hanessian V, Jensen TK, Nielsen J, Sureda M, Kataria D, Belkouchi B, Conte A, Seminari S, Road O, Deimos E, Systems S, Space M (2021) Design, Set-Up, and First Ignition of the RF Helicon-based Plasma Thruster. In: *Space Propulsion Conference 2020+1*. [https://www.researchgate.net/publication/350124196\\_Design\\_Set-Up\\_and\\_First\\_Ignition\\_of\\_the\\_RF\\_Helicon-based\\_Plasma\\_Thruster](https://www.researchgate.net/publication/350124196_Design_Set-Up_and_First_Ignition_of_the_RF_Helicon-based_Plasma_Thruster)
3. Takahashi K, Takao Y, Ando A (2020) Increased Thrust-to-Power Ratio of a Stepped-Diameter Helicon Plasma Thruster with Krypton Propellant. *J Propuls Power*. <https://doi.org/10.2514/1.J054179>
4. Takahashi K, Sugawara T, Ando A (2020) Spatial measurement of axial and radial momentum fluxes of a plasma expanding in a magnetic nozzle. *New J Phys* 22(7):0–9. <https://doi.org/10.1088/1367-2630/ab98d5>

5. Takahashi K (2021) Magnetic nozzle radiofrequency plasma thruster approaching twenty percent thruster efficiency. *Sci Rep* 11(1):1–12. <https://doi.org/10.1038/s41598-021-82471-2>
6. Vinci AE, Mazouffre S (2021) Direct experimental comparison of krypton and xenon discharge properties in the magnetic nozzle of a helicon plasma source. *Phys Plasmas* 28(033504). <https://doi.org/10.1063/5.0037117>
7. Vinci AE, Mazouffre S (2021) Plasma properties conditioned by the magnetic throat location in a helicon plasma device. *J Appl Phys* 130(183301). <https://doi.org/10.1063/5.0069983>
8. Magarotto M, Manente M, Trezzolani F, Pavarin D (2020) Numerical Model of a Helicon Plasma Thruster. *IEEE Trans Plasma Sci*:1–10. <https://doi.org/10.1109/tps.2020.2982541>
9. Souhair N, Magarotto M, Ponti F, Pavarin D (2021) Analysis of the plasma transport in numerical simulations of helicon plasma thrusters. *AlP Adv* 11(115016). <https://doi.org/10.1063/5.0066221>
10. Merino M, Nuez J, Ahedo E (2021) Fluid-kinetic model of a propulsive magnetic nozzle. *Plasma Sources Sci Technol* 30(11):115006
11. Ahedo E, Merino M (2010) Two-dimensional supersonic plasma acceleration in a magnetic nozzle. *Phys Plasmas* 17(7):1–15. <https://doi.org/10.1063/1.3442736>
12. Takahashi K, Chiba A, Komuro A, Ando A (2016) Experimental identification of an azimuthal current in a magnetic nozzle of a radiofrequency plasma thruster. *Plasma Sources Sci Technol* 25(5):55011. <https://doi.org/10.1088/0963-0252/25/5/055011>
13. Merino M, Ahedo E (2015) Influence of electron and ion thermodynamics on the magnetic nozzle plasma expansion. *IEEE Trans Plasma Sci* 43(1):244–51. <https://doi.org/10.1109/TPS.2014.2316020>
14. Little JM, Choueiri EY (2016) Electron Cooling in a Magnetically Expanding Plasma. *Phys Rev Lett* 117(22):1–5. <https://doi.org/10.1103/PhysRevLett.117.225003>
15. Zhang Y, Charles C, Boswell R (2016) Thermodynamic Study on Plasma Expansion along a Divergent Magnetic Field. *Phys Rev Lett* 116(2):1–5. <https://doi.org/10.1103/PhysRevLett.116.025001>
16. Takahashi K, Charles C, Boswell RW, Ando A (2020) Thermodynamic Analogy for Electrons Interacting with a Magnetic Nozzle. *Phys Rev Lett* 125(16):165001. <https://doi.org/10.1103/PhysRevLett.125.165001>
17. Kim JY, Go G, Hwang YS, Chung KJ (2021) Dependence of the polytropic index of plasma on magnetic field. *New J Phys* 23(5). <https://doi.org/10.1088/1367-2630/abfab1>
18. Sudit ID, Chen FF (1994) RF Compensated Probes for High-density Discharges. *Plasma Sources Sci Technol* 3(2):162–168. <https://doi.org/10.1088/0963-0252/3/2/006>
19. Chen FF (2009) Langmuir probes in RF plasma: Surprising validity of OML theory. *Plasma Sources Sci Technol* 18(3). <https://doi.org/10.1088/0963-0252/18/3/035012>
20. Chen FF (2001) Langmuir probe analysis for high density plasmas. *Phys Plasmas* 8(6):3029–3041. <https://doi.org/10.1063/1.1368874>
21. Lobb RB, Beal BE (2017) Recommended practice for use of langmuir probes in electric propulsion testing. *J Propuls Power* 33(3):566–581. <https://doi.org/10.2514/1.835531>
22. Charles C (2010) High density conics in a magnetically expanding helicon plasma. *Appl Phys Lett* 96(5):13–16. <https://doi.org/10.1063/1.3309668>
23. Takahashi K, Akahoshi H, Charles C, Boswell RW, Ando A (2017) High temperature electrons exhausted from rf plasma sources along a magnetic nozzle. *Phys Plasmas* 24(8):0–4. <https://doi.org/10.1063/1.4990110>
24. Chen FF (2016) *Introduction to Plasma Physics and Controlled Fusion*. Springer. [https://doi.org/10.1007/978-3-319-22309-4\\_11](https://doi.org/10.1007/978-3-319-22309-4_11)
25. Burm KTAL, Goedheer WJ, Schram DC (1999) The isentropic exponent in plasmas. *Phys Plasmas* 6(6):2622–2627. <https://doi.org/10.1063/1.873535>
26. Collard TA, Jorns BA (2019) Magnetic nozzle efficiency in a low power inductive plasma source. *Plasma Sources Sci Technol* 28(10). <https://doi.org/10.1088/1361-6595/ab2d7d>
27. Dannenmayer K, Mazouffre S (2013) Electron flow properties in the far-field plume of a Electron flow properties in the far-field plume of a Hall thruster. *Plasma Sources Sci Technol* 22(035004). <https://doi.org/10.1088/0963-0252/22/3/035004>
28. Merino M, Fajardo P, Giono G, Ivchenko N, Gudmundsson JT, Mazouffre S, Loubère D, Dannenmayer K (2020) Collisionless electron cooling in a plasma thruster plume: Experimental validation of a kinetic model. *Plasma Sources Sci Technol* 29(3). <https://doi.org/10.1088/1361-6595/ab7088>
29. Bittencourt JA (2004) *Fundamentals of Plasma Physics*. Springer. <https://doi.org/10.1109/9780470544273.ch1>
30. Bellan PM (2006) *Fundamentals of Plasma Physics*. Cambridge University Press. <https://doi.org/10.1017/CBO9780511807183>

## Publisher's Note

Springer Nature remains neutral with regard to jurisdictional claims in published maps and institutional affiliations.